Split and delay photon correlation spectroscopy with a visible light

by

Marten Rasch

born on

28. October 1992

in Hamburg

Bachelor of Science, Physics

Universität Hamburg

Deutsches Elektronen-Synchrotron

handed in on:

21. February 2016

1. Gutachter: Prof. Dr. Gerhard Grübel
2. Gutachter: Prof. Dr. Andreas Stierle

Erklärung

Hiermit bestätige ich, dass die vorliegende Arbeit von mir selbständig verfasst wurde und ich keine anderen als die angegebenen Hilfsmittel - insbesondere keine im Quellenverzeichnis nicht benannten Internet-Quellen - benutzt habe und die Arbeit von mir vorher nicht einem anderen Prüfungsverfahren eingereicht wurde. Die eingereichte schriftliche Fassung entspricht der auf dem elektronischen Speichermedium. Ich bin damit einverstanden, dass die Bachelorarbeit veröffentlicht wird.

_____   _____
Ort, Datum   Marten Rasch

Abstract

The development and performance of a setup constructed with the aim for the split pulse photon correlation spectroscopy is presented in this thesis. The double pulse time structure is accomplished with help of an Acusto-Optic Modulator (AOM) crystal, which mimics the splitting and delaying of photon pulses. The setup provides double pulses and allows to control the pulse width and delay and to synchronize them into one camera exposure window. The performance of the setup was successfully verified in a proof of principle experiment with a model system of polystyrene particles following Brownian motion. The measured radius of particles obtained with from the split pulse experiment ($R_h = (2.567 \pm 0.097)\,\mu\text{m}$) is in agreement with the particle size provided by the manufacturer ($R = (2.26 \pm 0.08)\,\mu\text{m}$). The achieved results show higher statistics compared to a standard Dynamic Light Scattering (DLS) measurement.

Zusammenfassung

Die Entwicklung und Leistungsfähigkeit eines Messaufbaus, für Doppelpuls Photonen Korrelation Spektroskopie wird im Rahmen dieser Arbeit präsentiert. Eine zeitliche Doppelpuls Struktur wurde mit der Hilfe eines Akusto Optischen Modulators hergestellt, welcher die Aufteilung und Verzögerung von Lichtpulsen nachahmt. Um ein solches Pulsverzögerungs Experiment durchzuführen, bietet der Aufbau die Möglichkeit, die Pulsbreite und die Verzögerung des Doppelpulses zu kontrollieren. Dieser Doppelpuls kann dann mit der Kamera aufgenommen werden und die Veränderung des speckle-Musters als Funktion der Zeit zwischen den beiden Lichtpulsen analysiert werden. Die Bewegungen von Polystyrol Partikeln in Wasser können durch Brownsche Molekularbewegungen beschrieben werden und der mit dem Doppelpuls Experiment gemessene Partikelradius ($R_h = (2.567 \pm 0.097)\,\mu m$) stimmt gut mit den Angaben des Herstellers ($R = (2.26 \pm 0.08)\,\mu m$) überein. Die ermittelten Ergebnisse zeigen eine höhere Genauigkeit im Vergleich zur Dynamic Light Scattering (DLS) Messung.

Contents

1 Introduction

Dynamic Light Scattering (DLS) [1] is a robust method to study the dynamics of nanometer sized particles dispersed in a solvent. In a DLS measurement one uses a point detector, which can acquire data at a fixed point in space with high dynamic range. An alternate detector choice is a 2-dimensional detector. The Charged-Coupled Device camera (CCD) is from the point of data size approximately one million point detectors, but has a lower acquisition rate compared the point detector. The rate of the frame acquisition gives the boundaries for particle dynamics, that can be detected. Using a point detector to collect the intensity of a speckle pattern limits the data to one small section of the speckle pattern. In order to improve statistics, one can measure over a large time period, but in the meantime, the sample can change its properties, e.g. due to sedimentation. Therefore, it is important, to collect a large amount of data points in a short time period with a higher acquisition rate. This can be accomplished with the double pulse technique [2], where the sample is illuminated with two following laser pulses and those two illuminations are taken into one camera exposure. The setup mimics a split and delay technique which was employed for Free Electron Lasers (FEL) [3]. The larger the delay, the more a dynamical speckle pattern has changed after the first illumination and the lower is the contrast of the resulting frame [2]. The time between those two pulses, the time delay, has an effect on the contrast of the speckle pattern. The delay is provided by an Acusto-Optic Modulator (AOM), which produces timed and triggered diffraction orders. The diffraction occurs inside a crystal using sound waves. With this component, one can produce timed illuminations on the CCD, as it is sketched in Fig.1.1.
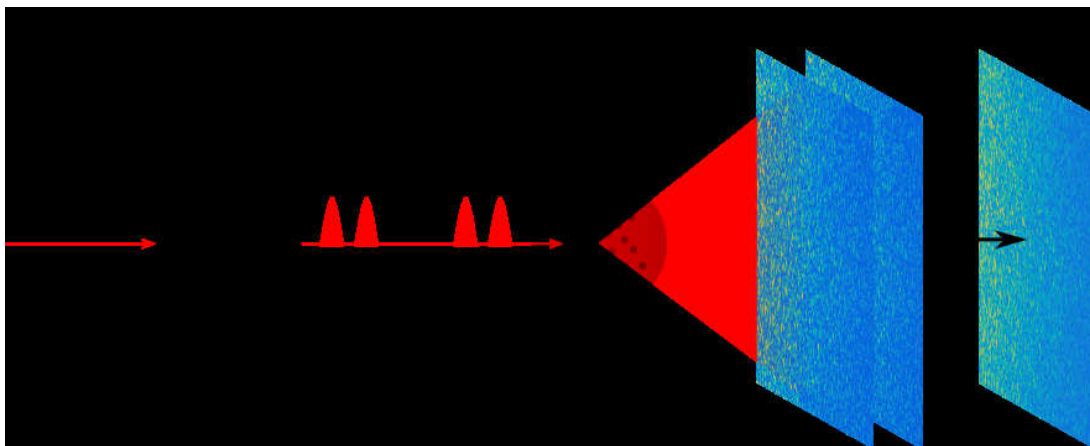

Figure 1.1: Double pulse experimental scheme. The AOM produces two single laser pulses with a lag time τ. The two light pulses scatter from a sample and produce two speckle patterns, that are summed in the CCD camera to one image.

It is possible to compare the contrast values of the delay data with the single shot autocorrelation function. The fastest particle dynamics, that can be analysed with time autocorrelation, is limited by the camera's frame rate. It is also possible to use the double pulse technique to

get the autocorrelation function, but the camera exposure time limits the maximal delay time. Therefore, slow dynamics is better analysed from autocorrelation data taken with a CCD. In this thesis it will be shown, that the information one gets from the autocorrelation setup is equivalent to the double pulse correlation technique.

The main task of this thesis was to set up the double pulse photon correlation system for studying dynamics of nanometer size colloidal particles with a 2D detector. This included building and testing the components, especially the AOM, and constructing a sample environment and investigating the stability of the laser source. Also the analysis programs had to be written. The theoretical background for the analysis of autocorrelation and double pulse speckle contrast data is presented in section 2. The experimental setup, including the description of the AOM is given in chapter 3. Chapter 4 shows the analysis of the measured data. Chapter 5 presents the results of the measurement period. The performance of the double pulse setup was successfully verified with a model system of polystyrene particles.

2   Theory

This section summarizes and explains the used equations for Dynamic Light Scattering (DLS) and later for double pulse correlation spectroscopy.

2.1   Basic Light Scattering Theory

Considering only a nonmagnetic, nonconducting, nonabsorbing medium with average dielectric constant ϵ_0, we can define an electrical field in the form of a plane wave

$$\mathbf{E}_i = \mathbf{n}_i E_0 e^{i(\mathbf{k}_i \cdot \mathbf{r} - \omega_i t)} \tag{2.1}$$

with $\mathbf{n}_i$ the unit vector in the direction of the incident field, the field amplitude E_0, the wave vector $\mathbf{k}_i$ and its frequency ω_i, illuminating a volume with density $\rho(\mathbf{r})$. The scattered electrical field takes in the far field approximation the form

$$E_f(\mathbf{r}') = \mathbf{E}_i e^{i\mathbf{k}_i \mathbf{r}'} + \mathbf{E}_i \frac{e^{i\mathbf{k}_i \mathbf{r}'}}{\mathbf{r}'} r_0 \int_{Vol} \rho(\mathbf{r}) e^{i\mathbf{q}\mathbf{r}} d^3 r \tag{2.2}$$

with the classical electron radius r_0. The integral is defined as the form factor amplitude $F(\mathbf{q})$

$$F(\mathbf{q}) = \int_{Vol} \rho(\mathbf{r}) e^{i\mathbf{q}\mathbf{r}} d^3 r. \tag{2.3}$$

In these equations, q describes the wave vector transfer $\mathbf{q} = \mathbf{k}_s - \mathbf{k}_i$, where $\mathbf{k}_{s/i}$ denotes the wave vector of the incident and the scattered light. Elastic scattering assumes, that $|\mathbf{k}_s| = |\mathbf{k}_i|$. In this approximation the modulus of the wave vector transfer is given by

$$|q| = q = |\mathbf{k}_s - \mathbf{k}_i| = \frac{4\pi n}{\lambda} \sin \frac{\Theta}{2} \tag{2.4}$$

where λ is the wavelength, n the index of refraction of the sample and Θ the angle between $\mathbf{k}_i$ and $\mathbf{k}_s$ [1].

From the experimental point of view, the factor $\frac{r}{D}$ can be substituted for $\sin \frac{\Theta}{2}$ which leads to

$$q = \frac{4\pi n}{\lambda} \cdot \frac{r}{D} \tag{2.5}$$

with r being the distance between the scattered light and the beam center in real space and D is the distance between sample and camera. This equation is later used to get the specific q value in reciprocal space. The refractive index n, denotes the light diffraction of the sample container. For dilute samples, it can be approximated with the refractive index of water.
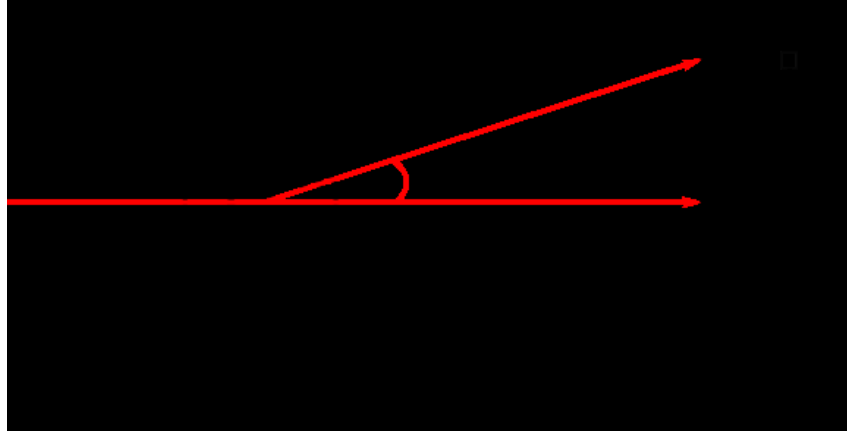
Figure 2.1: Scheme of q space derivation

Using the definition of the form amplitude, one arrives at the formula for the differential cross section

$$\frac{d\sigma}{d\Omega}(\mathbf{q}) = r_0^2 F(\mathbf{q})F(\mathbf{q})^* \tag{2.6}$$

with the classical electron radius r_0. For the scattered intensity follows

$$I(\mathbf{q}) = I_0 \frac{1}{L^2}\frac{d\sigma}{d\Omega}(\mathbf{q}) \tag{2.7}$$

where L denotes a characteristic dimension of the scattering volume. $I_0 = E_0^2$ gives the intensity of the incident wave. The next step is to go from a general distribution, to a system of $\bar{N}$ identical and spherical particles in the illuminated sample volume. It is assumed, that the sample is diluted enough to exclude multiple scattering. For the form factor amplitude $F_1(q)$ of a single particle

$$F_1(\mathbf{q}) = \int_{Vol} \rho^p(\mathbf{r})e^{i\mathbf{dr}}d^3\mathbf{r} \tag{2.8}$$

where ρ^p is the scattering centre distribution within one particle. The total density within the scattering volume is

$$\rho(\mathbf{R}) = \sum_{j=1}^{\bar{N}} \rho^p\left(\mathbf{R} - \mathbf{R}_j\right), \tag{2.9}$$

where $\mathbf{R}_j$ describes the centre of the particle j. The total form amplitude is now given by

$$F(\mathbf{q}) = \sum_{j=1}^{\bar{N}} F_1(\mathbf{q})e^{i\mathbf{q}\mathbf{R}_j}. \tag{2.10}$$

Making use of formula (2.6), (2.7) and (2.10), the scattered intensity can be written as

$$I(\mathbf{q}) = I_0 \frac{r_0^2}{L^2} \bar{N} P(\mathbf{q}) S(\mathbf{q}) \tag{2.11}$$

with the formfactor $P(\mathbf{q})$, the structure factor $S(\mathbf{q})$ and the incident intensity I_0. The formfactor describes the scattering from each particle and is given by

$$P(\mathbf{q}) = |F_1(\mathbf{q})|^2 . \tag{2.12}$$

2.2 Correlation Functions

The analysis of speckle patterns, arising from coherent light scattering experiments, is based on time correlations. The theory of correlation functions discussed in this chapter is based on [1]. A statistical signal or function $A(t)$ at the time t can be averaged over time by

$$\langle A(t) \rangle_t = \langle A \rangle_t = \lim_{T \to \infty} \frac{1}{T} \int_t^T A(t') dt' \tag{2.13}$$

with the total time T. A continuous measurement of A is not possible, due to the technical properties of detectors. Therefore, the acquisition is divided into N signals at the times t_j. Now the average is approximated by the sum of all signals divided by N [1].

$$\langle A \rangle_t = \lim_{N \to \infty} \frac{1}{N} \sum_{j=1}^{N} A(t_j) . \tag{2.14}$$

For inspecting the correlation between two signals at time 0 and time τ, the average is extended to

$$\langle A(0) A(\tau) \rangle = \lim_{N \to \infty} \frac{1}{N} \sum_{j=1}^{N} A(t_j) A(t_{j+1})$$

which simplifies in the limit of $\tau \to 0$ to $\langle A(0) A(0) \rangle_t = \langle A^2 \rangle_t$. This is the upper limit for correlation functions, that means the correlation between to identical signals. The lower limit, $\tau \to \infty$ leads to

$$\langle A(0) A(\tau \to \infty) \rangle_t = \langle A(0) \rangle_t \langle A(\tau) \rangle_t = \langle A \rangle_t^2. \tag{2.15}$$

Therefore, the degree of correlation is limited as follows

$$\langle A^2 \rangle \le \langle A(0) A(\tau) \rangle \le \langle A \rangle^2. \tag{2.16}$$

The autocorrelation function $\langle A(0) A(\tau) \rangle$ decays like a single exponential function between those two values, dependent on the dynamics of e.g. a colloidal systems [1].

In light scattering experiments, the statistical signal will be additionally dependent on the wavevector transfer q, which will be part of the explanation in the following chapter.

2.3 Dynamic Light Scattering

The analysis of DLS data for relatively slow processes on timescales slower than the frame rate of the detection system is as follows. In the DLS measurement one records the fluctuating intensity, which is further processed according to the normalized intensity correlation function given by

$$g_2(\mathbf{q}, t) = \frac{\langle |I(\mathbf{q}, 0)| \, |I(\mathbf{q}, t)| \rangle}{\langle |I(\mathbf{q})| \rangle^2} \tag{2.17}$$

with $I(\mathbf{q}, t)$ denoting the intensity at specific $\mathbf{q}$ and time t. This can be rewritten with the Siegert relation for Gaussian signals to

$$g_2(\mathbf{q}, t) = 1 + \beta^2 |g_1(\mathbf{q}, t)|^2. \tag{2.18}$$

Due to experimental factors, the coherence factor β^2 is introduced, which is from an experimental point of view a contrast. This factor depends on limited coherence of the laser and can be reduced by any instabilities of the experimental setup [1]. It is further explained in Chapter 2.4.

2.3.1 Diffusion

In this work, only dilute sample solutions of large particles in the micrometre regime are considered. Their dynamics are assumed to be only Brownian motion with independent translational movement, where the movement at any point in time is independent of the movement and position at any earlier point in time [1]. An interaction with the sample holder is avoided, by selecting a scattering volume in the middle of the sample holder. Any parasitic scattering was excluded from the analysis. The diffusion equation is given by [1]

$$\frac{\partial P(\mathbf{r}, t)}{\partial t} = D_0 \nabla^2 P(\mathbf{r}, t) \tag{2.19}$$

where $P(\mathbf{r}, t)$ is the probability density of a single particle being located at $\mathbf{r}$ at the time t and D_0 is the self diffusion coefficient for a spherical particle. D_0 is given by the Stokes-Einstein relation

$$D_0 = \frac{k_b T}{6\pi \eta R_h} \tag{2.20}$$

with the temperature T, the Boltzmann constant k_b, the solvent viscosity η and the (hydro-dynamical) radius R_h of the particles. The hydrodynamical radius can be obtained by DLS measurement and describes the radius of a hypothetical spherical particle, which diffuses with a diffusion constant D_0 given by Eq.2.20. The particles used in this thesis, are stated to have a spherical shape [4].

2.3.2 Intermediate scattering function

Making use of the Siegert relation for Gaussian signals, the time autocorrelation function can be written as

$$g_2(\mathbf{q}, t) = 1 + \beta^2 |f(\mathbf{q}, t)|^2 \tag{2.21}$$

with the normalized intermediate scattering function $f(\mathbf{q}, t)$. The intermediate scattering function for Brownian particles is given by [5]

$$f(\mathbf{q}, t) = \exp(-\mathbf{q}^2 D_0 t). \tag{2.22}$$

Therefore, $g_2(\mathbf{q}, t)$ can expressed in terms of the diffusion coefficient D_0 as follows

$$g_2(\mathbf{q}, t) = 1 + \beta^2 e^{-2\Gamma t}, \tag{2.23}$$

where β^2 denotes the single shot contrast and Γ is the relaxation rate Γ given by

$$\Gamma = q^2 D_0 = \frac{1}{\tau_0}. \tag{2.24}$$

τ_0 in Eq.2.24 is the relaxation time or the time, after which the g_2 function decays to $(1/e)$.

2.4   Double Pulse Speckle Contrast

In a double pulse experiment the sample is illuminated coherently with two pulses separated by the delay time τ. The scattering intensity is collected by the CCD as summed intensity $S(\mathbf{q}, \tau)$ [2]

$$S(\mathbf{q}, \tau) = I(\mathbf{q}, t_i) + I(\mathbf{q}, t_i + \tau) \tag{2.25}$$

where $I(\mathbf{q}, t_i)$ denotes the intensity at the time t_i. Therefore, $S(\mathbf{q}, \tau)$ is the summed intensity of both pulses.

The contrast β^2 of a speckle pattern is given by [6]

$$\beta^2 = \frac{\sigma^2(I)}{\langle I \rangle^2} \tag{2.26}$$

with the variance $\sigma^2(I)$. The ideal single shot contrast β^2 equals 1 for a fully coherent beam. The normalized variance of $S(\mathbf{q}, \tau)$ denotes the contrast of a double pulse image over delay time τ

$$c_2(\mathbf{q}, \tau) = \frac{\langle S^2(\mathbf{q}, \tau) \rangle - \langle S(\mathbf{q}, \tau) \rangle^2}{\langle S(\mathbf{q}, \tau) \rangle^2} \tag{2.27}$$

where c_2 for small τ in the regime of the pulse width can be approximated as single shot contrast β^2. $c_2(\mathbf{q}, \tau)$ drops down from β^2 for adding two identical images to $\frac{1}{2}\beta^2$ for adding two completely uncorrelated images. This is shown in Fig.2.2b.

For a fully coherent source, the double pulse contrast $c_2(\mathbf{q}, t)$ can be rewritten to $c_2(\mathbf{q}, \tau) = \frac{1}{2}\left(1 + |f(\mathbf{q}, \tau)|^2\right)$. A derivation can be found in the appendix A.1. Taking the effects of coherence (β^2) into account, the double pulse contrast is

$$c_2(\mathbf{q}, \tau) = \frac{\beta^2}{2}\left(1 + |f(\mathbf{q}, \tau)|^2\right). \tag{2.28}$$

With the g_2 function from Eq.2.17

$$g_2(\mathbf{q}, \tau) = 1 + \beta^2 |f(\mathbf{q}, \tau)|^2, \tag{2.29}$$

Now one can see, that the information one gets from the autocorrelation can be compared to the double pulse contrast information by

$$g_2(\mathbf{q}, \tau) - 1 = 2c_2(\mathbf{q}, \tau) - \beta^2. \tag{2.30}$$

A comparison of c_2 and g_2 is illustrated in Fig.2.2a and 2.2b with calculated experimental data. Fig.2.2a shows the g_2 function as a function of delay time τ for different contrast values. In the case of the highest contrast of $\beta^2 = 1$, the g_2 function decays from 2 to 1. In Fig.2.2b one can

see, that with the highest contrast, the function goes from 1 to 0.5 and the higher the contrast β^2, the steeper the drop of the function. With equation 2.30 it is possible to plot both data into one graph, which is shown in Fig.2.3. That means it is possible, to transform c_2 into a g_2-plot and do the fit of Eq.2.23. The equation is applicable at lower values of contrast, what can be seen in Fig.2.3 in the lower contrast functions $\beta^2 = 0.9$ and $\beta^2 = 0.8$.
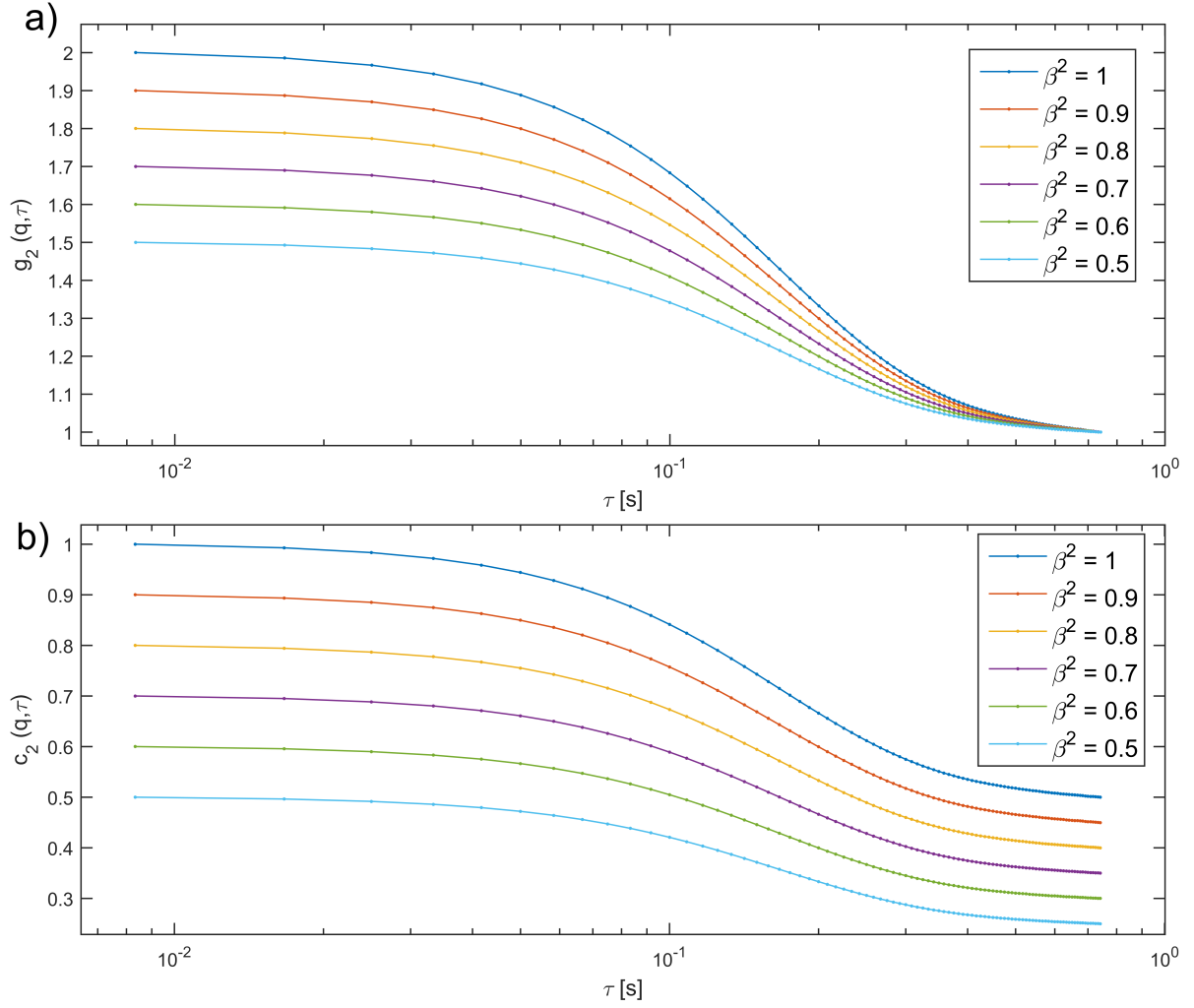
Figure 2.2: Comparison of **a)** $g_2(\mathbf{q}, \tau)$ and **b)** $c_2(\mathbf{q}, \tau)$ and their dependence on β^2
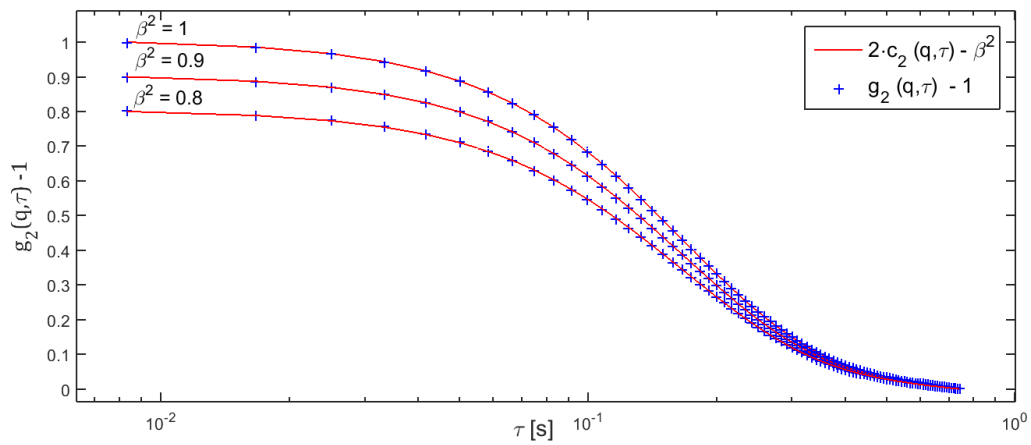
Figure 2.3: Equivalence of g_2 and c_2 with using Eq.2.30 for different β^2.

2.5 Speckle Pattern

This chapter focuses on the spatial distribution of the scattered coherent light, called speckle pattern. A speckle pattern is a random diffraction pattern and generated, when coherent light impinges on a disordered system. While a conventional DLS setup uses point detectors, the 'multispeckle analysis' with a CCD chip with an edge length of several millimetres takes a bigger sector into account. With this technical advantage, the fluctuations of a big number of speckles are analysed. It is also possible, to extract information about the speckle contrast, which is related to the degree of coherence of the laser setup, as well as the radial size of the beam at the position of the sample, as described in the following.

Assuming again full coherence, the intensity probability distribution of the speckle pattern is given in terms of the mean intensity by an exponential distribution

$$P(I) = \frac{1}{\langle I \rangle} e^{-\frac{I}{\langle I \rangle}}. \tag{2.31}$$

In addition the size of a single speckle can be calculated by

$$\delta_{x,y} = \lambda \frac{L}{D_{x,y}} \tag{2.32}$$

where $\delta_{x,y}$ is the full width half maximum in horizontal (x) or vertical (y) direction. $D_{x,y}$ is the effective scattering region, that is illuminated and L the sample-detector distance. One can see in the Equation 2.32, that the speckle size is independent of the particle size, but several factors can change the dimensions of the speckle. This is further discussed in the section 5.4.

3 Experimental

3.1 Setup

Parameter	HeNe laser
Wavelength λ	632.8 nm
Power P	2.0 mW
Beam diameter ($^1/e^2$)	0.81 mm
Beam divergence	1.0 mrad
Polarization	random

Table 3.1: Specifications of HeNe laser HNL020R-EC from Thorlabs GmbH [7]

In this section I will describe the setup, as sketched in Fig.3.1, starting from the laser. The source is a Helium-Neon-laser of the company Thorlabs GmbH. The specifications of this laser can be found in the Table 3.1. After two mirrors for directing the beam into the AOM, the AOM splits the beam into diffraction orders as shown in Fig.3.2. The main beam will be blocked at the iris and the first diffraction order beam will pass. This beam is now timed by the DDG. A second iris blocks some stray light to keep the beam small and clean. A first plain convex lens with a focal length of 50.0 mm focuses the beam. The beam is now directed through a aperture in the cover of the black cover box (see Fig.6.2). This aperture is held small enough, to avoid background light on the detector, but not too small to produce a new interference source. Now the beam is inside the black cover box focused on the sample. The sample is contained in a quartz cuvette (see Fig.3.4) manufactured by Thorlabs GmbH [8] on a motor stage orthogonal to the beam. The reason for this stage, is to position the sample exactly with the beam in the center of the cuvette. Once the beam scatters at the sample, the pattern is refocused by a 100.0 mm lens on the camera. The direct beam is blocked by a small black screw, which acts as a beamstop. To avoid saturation on the camera, one can select an attenuator, or lower the pulse width via the Digital Delay Generator (DDG). The specifications of the camera are shown in the Table 3.2. The camera is also fixed on a motor stage, which provides horizontal movement in a 90-degree-orientation, to acquire different q-values.

Parameter	Basler avA1000-120km
Pixel	1024×1024 (1040×1040 max)
Pixel Size	$5.5 \times 5.5 \, \mu m$
Dynamic range	8-, 10-, 12-bit (8-bit used)
Max. frame rate	120 fps
Exposure time	$12 \, \mu s$ to 2.5 s
Sensor type	Kodak KAI-1050
Sensor techn.	Progressive scan CCD, global shutter

Table 3.2: Specifications of Basler Aviator avA1000-120km CCD camera [9]

Figure 3.1: Scheme of the setup, with the Wavefunction Generator (WFG), the Acusto-Optic Modulator (AOM) and the Digital Delay Generator (DDG)

Parameter	AOM specifications
Interaction Material	Crystal Quartz
Wavelength	$400 - 540\,\mathrm{nm}$
Optical polarisation	Linear, vertical to base
Transmission (single pass)	$> 99\%$
RF frequency	$110\,\mathrm{MHz}$
Separation angle	$10.2\,\mathrm{mrad}$ at $532\,\mathrm{nm}$
Diffraction Efficiency	$> 85\%$

Table 3.3: Specifications of the Gooch & Housego Acousto-Optic Modulator I-M110-3C10BB-3-GH27 [10]

Over a PCI-1428 card and PCI cable the camera is connected with the computer and frames are acquired with the program "National Instruments Vision Assistant 2011". To set up the camera options, the program "Pylon Viewer 4.0" from Basler AG was used. With a hirose pin cable the camera was connected to the Wavefunction Generator (WFG) (*Tektronix AFG3022C*) to receive the trigger signal at the rising edge. From the same output channel, the WFG was connected with a $50\,\Omega$-cable to the Digital Delay Generator (DDG) (*Stanford Research Systems Model DG645*). The time chart can be seen in Fig.3.3. For diagnostics purposes the signals of the AOM and the CCD additionally observed on a two-channel oscilloscope (*Hameg HM1507-3*). In the process of building up the system, it was useful to have a visual feedback of the signal flow.

In a double pulse operation mode, the DDG gives two triggered $1\,\mathrm{Volt}$-signals to a Radio Frequency driver (*Gooch & Housego A35110-S-1/50-p4k7u*), which generates the acoustic wave at $110\,\mathrm{MHz}$ for the AOM. The RF driver is mounted on a cooling element to avoid heating damage. These radio waves from the RF Driver are transmitted to the AOM crystal (*Gooch & Housego I-M110-3C10BB-3-GH27*[10]) via a SMA cable and create a static wave on a quartz crystal (Fig.3.2). At this static wave, the beam diffracts and produces diffraction orders with a high transmission rate up to 85% of the input [10]. The first diffraction order is now used as the main beam. In this way, one can split the beam into single triggered and timed pulses and synchronize these pulses with a camera shutter. The Table 3.3 shows the specifications of the used AOM.

Even though the experimental wavelength is $632.8\,\mathrm{nm}$, which is out of the specification range, the AOM was still operating, however with losses in intensity. The AOM is mounted on a rotation stage, to ensure a orthogonal incoming beam.

Figure 3.3 shows a time flow of the three most important signals. The top one is a $5\,\mathrm{V}$-square pulse function generated by a WFG to trigger the camera and the DDG, which controls the Acusto-Optic Modulator (AOM). The above mentioned time was implemented to verify the simultaneous acquisition and pulsing, triggered by the rising edge of the square pulse. The camera has an internal delay of $42\,\mu\mathrm{s}$ [9], plus several nanosecond delays (due to cable length) after the triggering. To make sure, that the double pulse does not set in too early, a delay of $100\,\mu\mathrm{s}$ was set before the pulses. The pulse width of the CCD was set equal to the trigger func-

tions width. The camera exposure was set to a minimum length to acquire just the double pulse and to keep the background light low, although the background was subtracted via the dark frames in every measurement. It was also recognized while measuring a static silica sample, that the system is sensitive to the air conditioning. A housing was built around the sample position. To minimize the background light, this housing was covered in black cloth with a small aperture for the beam. Several images of the setup can be found in the appendix A.2 under Fig.6.1 to Fig.6.3.
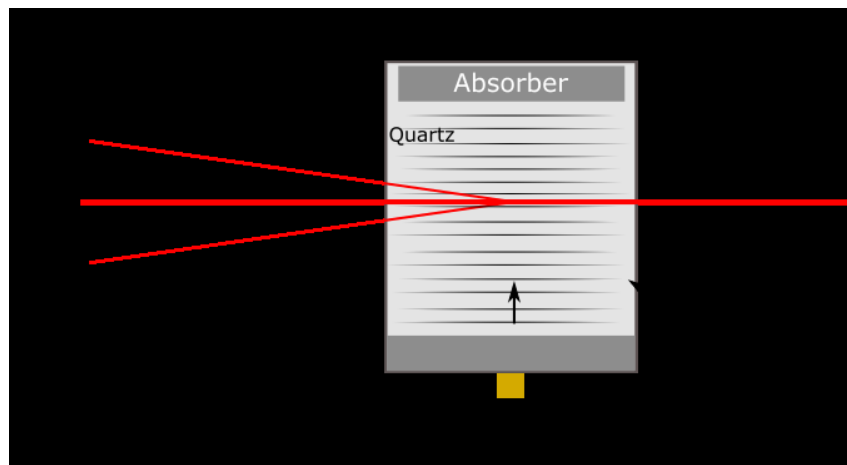
Figure 3.2: The concept of an AOM. The incoming beam from the right, diffracts on the sound waves in the radio frequency range, produced by the RF Driver and transmitted through the SMA cable to the AOM, and diffraction orders occur inside the quartz crystal. The diffraction orders are now timed and triggered. The sound waves are absorbed afterwards.
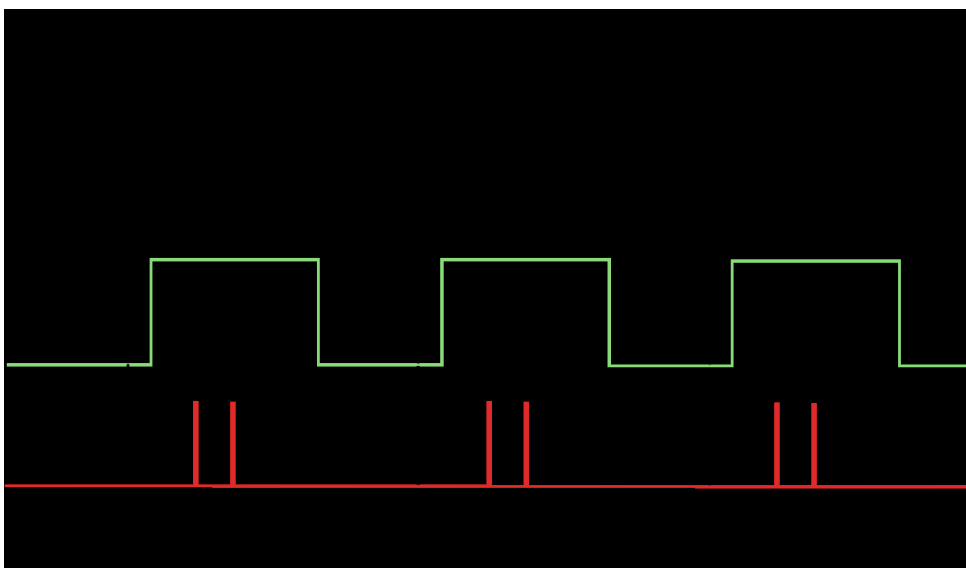
Figure 3.3: Overview over the trigger and signal time flow. The Wavefunction Generator (WFG) triggers the Acusto-Optic Modulator (AOM) and the Charged-Coupled Device camera (CCD).

3.2   Sample Preparation

Parameter	Polystyrol Microspheres
Description	Polybead® Polystyrene 4.5 Micron Microspheres [9003-53-6]
Manufacturer	Polyscience, Inc.
Diameter	$4.52 \pm 0.15\,\mu\mathrm{m}$
Solution proportion	$5\,\mu l$ particle fluid to $3000\,\mu l$ water
Coefficient of Variance (CV)	7%

Table 3.4: Sample specifications of Polybead® Polystyrene 4.5 Micron Microspheres [4].

The cuvette (see Fig.3.4) was flushed a couple of times and cleaned with water in an ultrasonic bath or new cuvettes of the manufacturer were used. Only pure water was used, to avoid parasitic scattering sources. After cleaning and drying the cuvette, the sample fluid was mixed and put into the ultrasonic bath, to ensure a complete mixing of water and particles and to dissolve possible compounds of multiple particles. After filling the fluid into the cuvette, a layer of Teflon paste was put onto the top of the cuvette, to seal the cuvette from evaporating and spilling out. After that, the top was also wrapped with Parafilm®. The experiment has shown, that only the top of the cuvette, even with Parafilm® wrapped around, did not prevent evaporation and due to sedimentation, the sample needed to be shaken before an experiment. Therefore, the cuvette needed to be impermeable. Later a different version of the cuvette with a stopper was used. Those cuvettes were already sealed against evaporation and spilling. To be sure, again a layer of Parafilm® was wrapped around the top.

Unless stated otherwise, spherical polystyrene particles with the specifications shown in Table 3.4 are used.

Figure 3.4: Sample cuvette from Thorlabs GmbH [8] with Parafilm® sealing

4   Data Analysis

The analysis of the collected data was performed with "MATLAB® R2015" and ran as followed. As the first step of each analysis, the dark frames were read in and a dark average frame was created. The amount of dark frames were around 10% of the measurement images.

The main measurement consists of one single pulse sequence with 100 frames and 30 double pulse sequences for each delay time. The single pulse sequence had in total the same pulse width per frame as the double pulse sequence, to achieve the same intensity. After subtracting the dark and excluding the negative entries by setting them to zero, the single pulse sequence was autocorrelated according to Eq.2.17. To achieve a proper time axis, the number of frames were divided by the camera frame rate.

Each double pulse sequence was also dark frame corrected and the contrast of each single image calculated according to Eq.2.27. For this calculation, the variance of pixel intensity values were divided by the mean squared. All contrast values of one sequence at a delay were averaged and the standard deviation of these approximated the statistical error. The factor β^2 was calculated by the single pulse contrast by Eq.2.27. The width of the pulses also determines the lower boundary for the delay time. The pulses originating from the AOM are no perfect square pulses. They can be compared on the rising and falling edge, with a Gaussian Curve. To ensure now a period of time between these two pulses, where the sample is not illuminated, the delay was set to more than twice the pulse width.

The estimated error of the contrast values were so small, that the error bars in plots like Fig.5.13 are smaller than the actual data point and therefore not visible. This can be explained by the statistics one gets by taking many images each with one million pixels. A comparison of the contrast by number of averaged images can be found in Fig.4.1. This plot shows on the one hand a clear dependence of the standard error on the number of frames and on the other hand a negligible change in the error after 50-100 frames. Even 25 images are enough, to keep the error under 1%. The contrast values are normalized to the contrast at 300 frames averaged. One can see, that the contrast also converges to 1 for larger numbers of summed frames.

To look more into the details of this error, it is plotted as a function of the number of images in Fig.4.2. One can see, that the error values in the regime of less than 10 images is relatively high, compared to higher frame numbers. So this range is not recommended to be used. For 10 frames, the error is smaller than 1.1% and the contrast is denotes about 3.5% off from 1. The range of the error in this plot is that small, that one can safely acquire small sequences with less than 50 images. Using the fit equation, displayed in Fig.4.2, one can calculate the error for 1 image, which is about 3.9%. The gain in error is negligibly small for higher frame numbers. For example for 1000 frames averaged, the error lies at 0.11%, which is about half of the error at 300 frames. It is recommended to mask out parasitic scattering and the shadow of the beamstop. These patterns are static and affect the contrast and are thus excluded from the analysis.
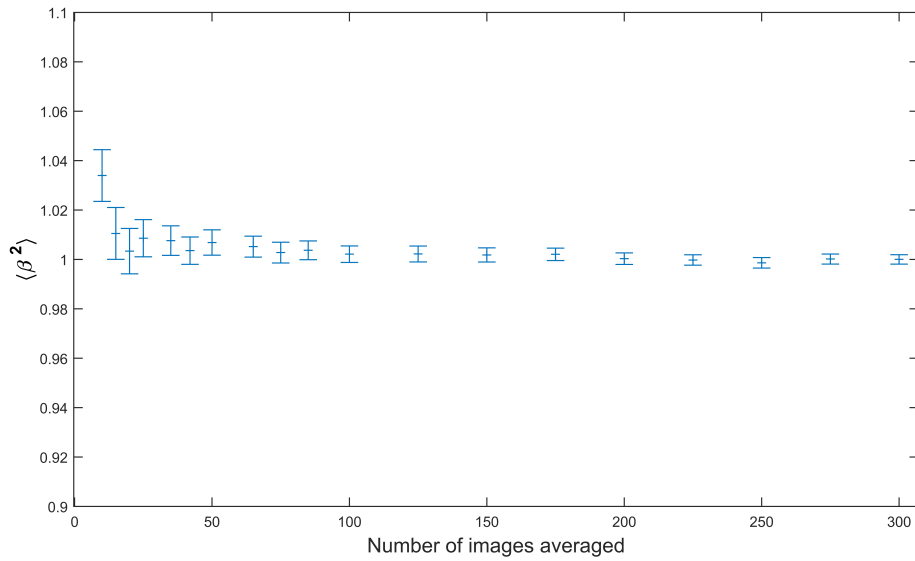
Figure 4.1: Normalized speckle contrast as a function of number of images averaged for $10\,\mu s$ single pulse at low q.
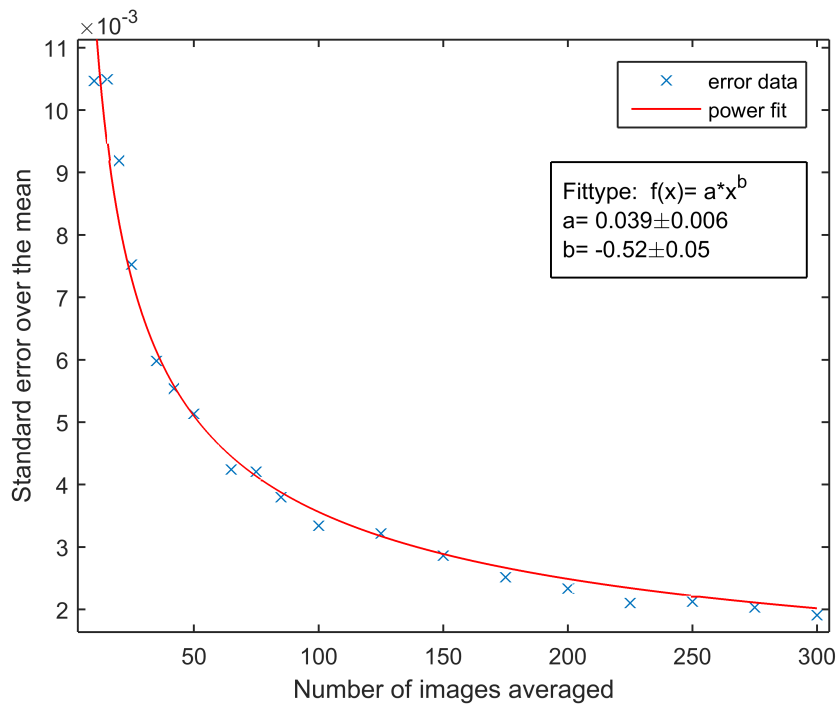

Figure 4.2: Standard error over the mean as a function of number of images for $10\,\mu s$ single pulse at low q inclusive a fit.

5   Results

5.1   Stability of experimental setup

In order to verify the stability of the experimental setup, the contrast of a static scattering pattern was measured. The sample consisted of $3.78\,\mu$m silica particles dried on a optical glass. The particles were dried with the drop cast technique onto the glass [11]. The optical glass was mounted on a combination of several rotation and translation stages, providing proper alignment to the laser beam.

The result of this short experiment was the unexpected observation of dynamics in the speckle pattern. This can be seen in the drop of the contrast as a function of the summed frames (see Fig.5.2). The decay of contrast indicates a certain instability of the setup. The measured contrast change occurs within the first 20 frames. The reason for this instability could be due to the air conditioning, which is located above the experimental setup. Although the optical table itself is stabilized and damped, certain vibrations or external stimulations could also trigger these dynamics. However, all these external instabilities reduce the contrast by approximately 2.5%, the setup can still be used and the external interferences are negligible small for measurements of colloidal dynamics.
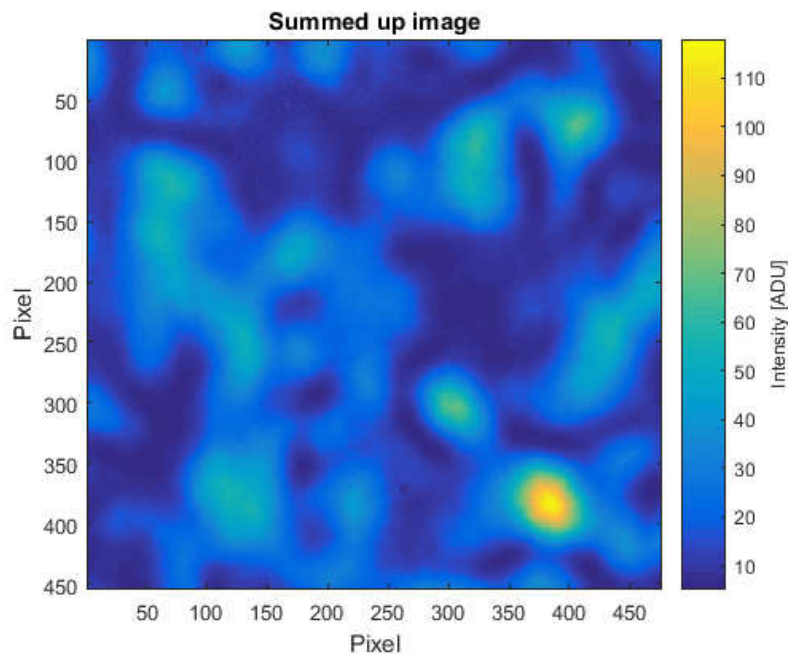
Figure 5.1: Speckle pattern of 1000 summed up frames taken with focused beam on static sample. The colorbar indicates the intensity recorded on th CCD in the intensity range from 0 to 115.
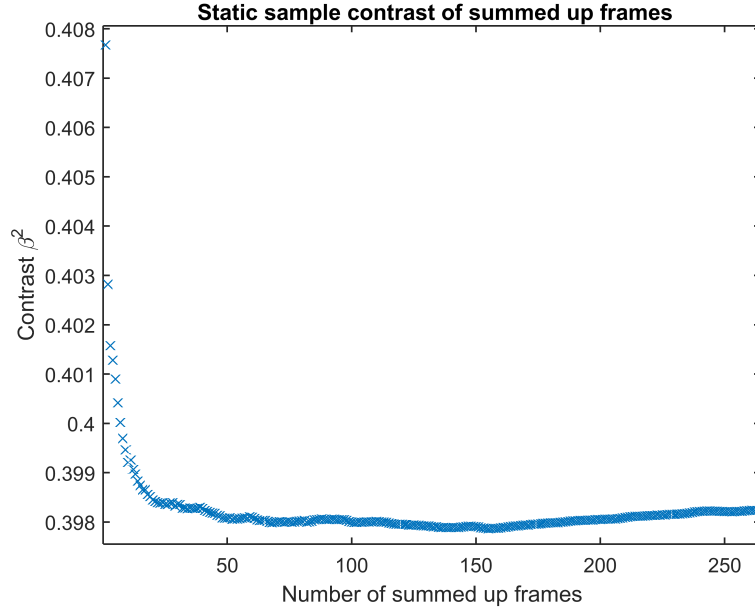
Figure 5.2: Contrast of summed single pulse frames at the static sample setup with dried silica particles.

5.2   Formfactor analysis

To access the momentum transfer $\mathbf{q}$ between the incident wave vector $\mathbf{k_i}$ and the scattered wave vector $\mathbf{k_s}$, the formfactor $F(\mathbf{q})$ has to be fitted to the normalized scattered intensity $I(\mathbf{q})/I(\mathbf{0})$ of a 2D image. The image was created, by stitching the images of 6 CCD positions together. The resulting image is shown in Fig.5.3a. The formfactor for spheres $F(\mathbf{q})$ can be calculated according to [12]

$$F(\mathbf{q}) = \frac{I(\mathbf{q})}{I(\mathbf{0})} = 9 \cdot \left(\frac{\sin(\mathbf{q}R) - \mathbf{q}R \cdot \cos(\mathbf{q}R)}{(\mathbf{q}R)^3} \right)^2 \tag{5.1}$$

where R is the particle radius. Fig. 5.3b shows the circularly averaged intensity $I(\mathbf{q})$. A clear differentiation of the maxima was not possible, so the effect of particle size polydispersity needed to be considered in the form of a polydispersity formfactor $F_\delta(\mathbf{q})$ given by [13]

$$F_\delta(\mathbf{q}) = \int_0^\infty \mathrm{d}R \, P(R) \cdot F(\mathbf{q}) \cdot \left(\frac{R}{R_0} \right)^6 . \tag{5.2}$$

The polydispersity $\delta = \Delta R / R_0$ is defined with the particle size width ΔR and the mean radius R_0 of a size distribution $P(R)$. This is given by the Schultz distribution function [14]

$$P_{(Z,R_0)}(R) = \frac{1}{Z!} \left[\frac{Z+1}{R_0} \right]^{Z+1} R^Z e^{-\frac{(Z+1)R}{R_0}} \quad \text{for } Z > -1 \tag{5.3}$$

The polydispersity δ is directly related to the parameter Z by

$$\delta = \frac{1}{\sqrt{Z+1}}. \qquad (5.4)$$

Since the distance between the sample and the camera was affected by the lens placed in between, the R_0 in the fit of the formfactor was set to $2.26\,\mu\mathrm{m}$. The fit parameter Z obtained of the formfactor fit is 80, giving a polydispersity of $\delta = 0.11$. The manufacturer of the particles states a size variance of 7%, which is close to the value, obtained from the fit.

The result of this fit is shown in Fig.5.3b. It provides the q value and the effective sample-CCD distance (affected by the lens in between sample and detector). The effective distance obtained from the fit is $L_{eff} = 15.5 \pm 0.1\,\mathrm{cm}$. Compared to the real measured distance of $L_{exp} = 9.4 \pm 0.1\,\mathrm{cm}$, the effective distance is 65% longer, which indicates that the speckle pattern is magnified. The resulting speckle sizes and beam sizes at both distances are compared in section 5.4.
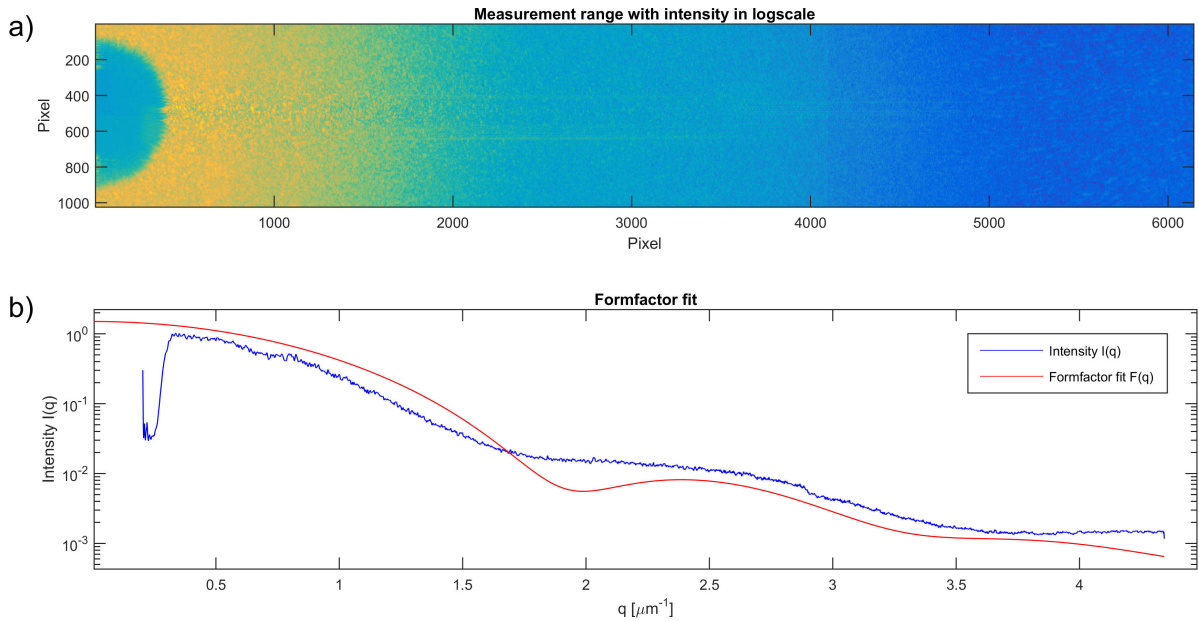
Figure 5.3: **a)** 2D image of the CCD range from beam to 6144 pixel. The resulting image consists of 6 neighbouring CCD positions stitched together via software.
b) The plot is the circular integral of the intensity $I(\mathbf{q})$ around the beam center. The red line denotes the corresponding fit.

5.3   Single Image Speckle Contrast

The main assumption of double pulse images is, that each of both shots produces one speckle pattern with the same contrast, independently of the q value. Thus the single shot contrast β^2 was measured. Several q-rings were selected on 30 single shot images, with masking of parasitic scattering and the contrast of each q-ring with Eq.2.26 calculated and averaged dependent on the q-value. The result is plotted in Fig.5.4. One can see, that the contrast is constant and close to 1. The fluctuations of the contrast at different q-values are small. Therefore, a illumination of $50\,\mu s$ is short enough, to get a static image without any smearing of the speckles. The brightness of the speckle pattern is proportional to the pulse width.

Unfortunately this short pulse width cannot be used at high q ranges, due to limited brightness. When increasing the pulse width to $20\,\text{ms}$, the contrast is 0.9 as shown in Fig.5.5. In case of longer illumination of the particles, the speckle pattern changes and therefore the contrast decreases. But one has to mention, that the scale of the contrast is again so narrow, that this effect within small q ranges is very small and within the error bars. The error bars are created by the standard error of 30 contrast values.
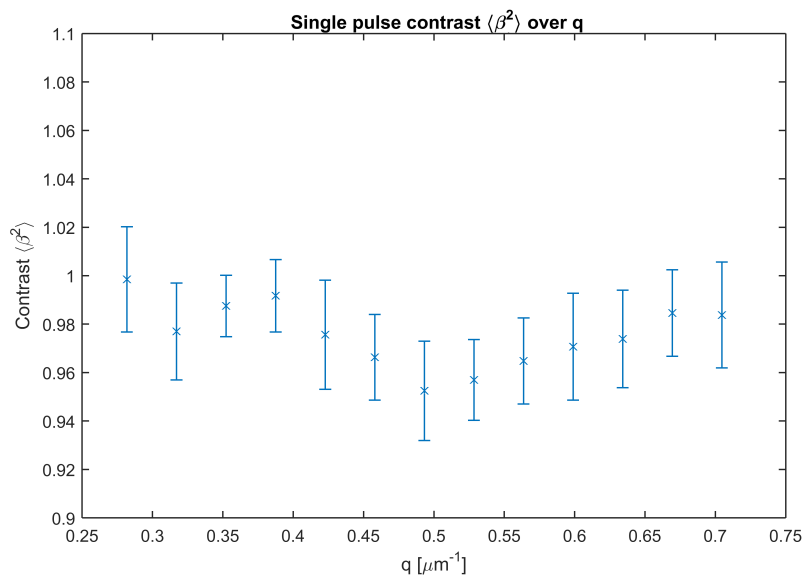
Figure 5.4: $50\,\mu s$ Single shot contrast over different q-values from $0.25\,\mu m^{-1}$ to $0.75\,\mu m^{-1}$, averaged over 30 frames
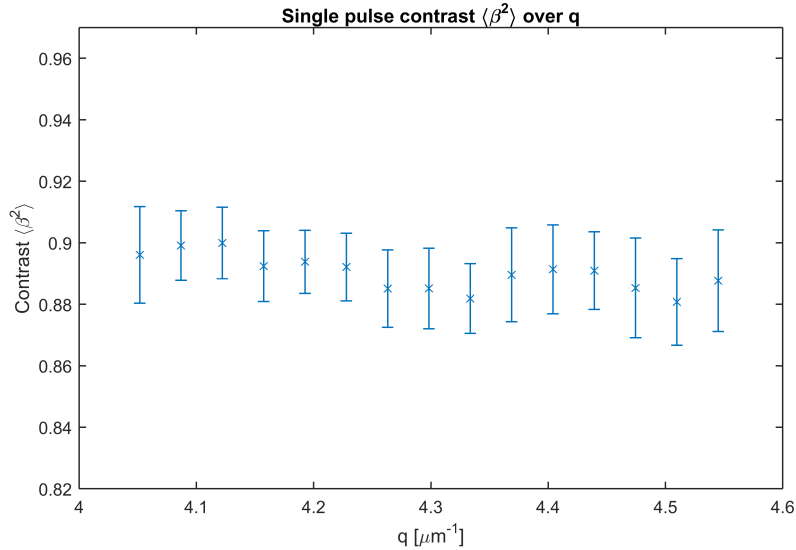
Figure 5.5: $20\,\mathrm{ms}$ single shot contrast at high q values from $4\,\mu\mathrm{m}^{-1}$ to $4.6\,\mu\mathrm{m}^{-1}$

5.4   Speckle Size

According to Eq.2.32, the speckle size is inversely proportional to the effective scattering region. In the case of single scattering and full coherence, the effective scattering region is simply the laser spot size at the position of the sample. The lens between sample and camera has a large influence on the beam size, which was calculated in chapter 5.2. With the effective distance of $15.5\,\mathrm{cm}$ the speckles appear larger, than they would do without the lens. Therefore, I will calculate the speckle size and the beam size in the following for both distances. Selecting speckles, that will be analysed, one has to select a region outside of any parasitic scattering, e.g. horizontal streak in the center of the image in Fig.5.6.

With Eq.2.32 one can calculate from the one-dimensional speckle size a horizontal and vertical beam size respectively. This is done with the spatial correlation function [15]

$$g(\delta_{x,y}) = \frac{\langle I(r + \delta_{x,y})I(r)\rangle}{\langle I\rangle^2}. \tag{5.5}$$

Figures 5.6 to 5.9 depicts one example of the speckle size analysis. With the cuts through the spatial correlation function and the corresponding Lorentzian fits, one can get the horizontal and vertical speckle size. The result of this calculation for one speckle is a effective lateral scattering region, or beam size, of $D_x = (115.27 \pm 1.27)\,\mu\mathrm{m}$ and $D_y = (128.93 \pm 1.27)\,\mu\mathrm{m}$. This speckle analysis was done at three different q-values $(0.14, 1.2, 4.0)\,\mu\mathrm{m}^{-1}$ for each 30 speckles to make the result more precise. The resulting speckle and beam sizes are plotted in Fig.5.10 and 5.11 with the effective distance $L_{eff} = 0.155\,\mathrm{m}$.

Fig.5.10 and 5.11 are not showing a direct linear dependence of the speckle size to the q value. Without taking the error into consideration, a slight trend to smaller speckle size at higher q is visible. This could be explained on the one hand with the aberration of the plain convex lens.
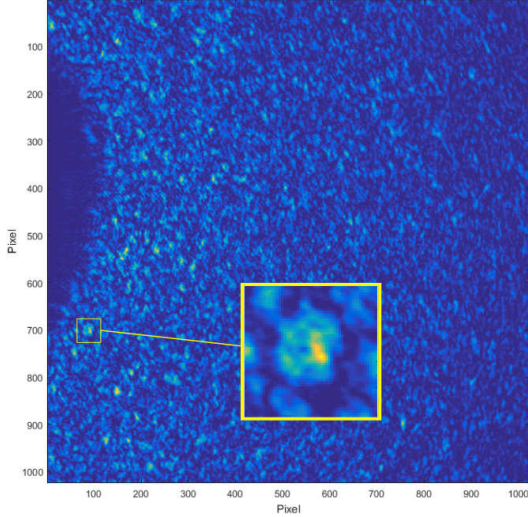
Figure 5.6: Example speckle pattern with a selected ROI (yellow square) of 50 pixel length
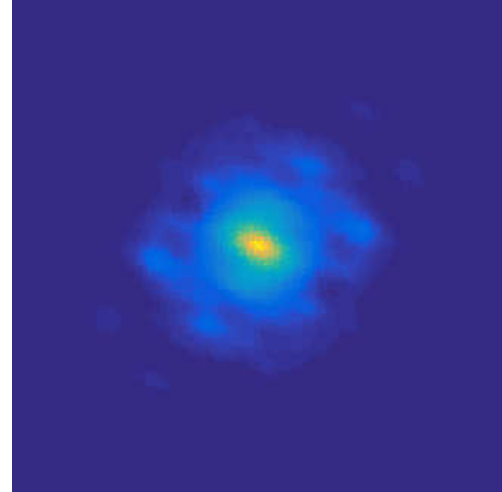

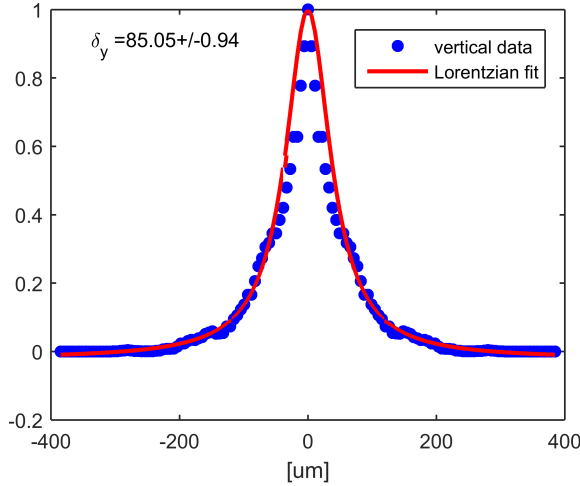Figure 5.7: Spatial autocorrelation function of ROI

Figure 5.8: Vertical cut through spatial correlation function with Lorentzian fit and the vertical speckle size δ_y
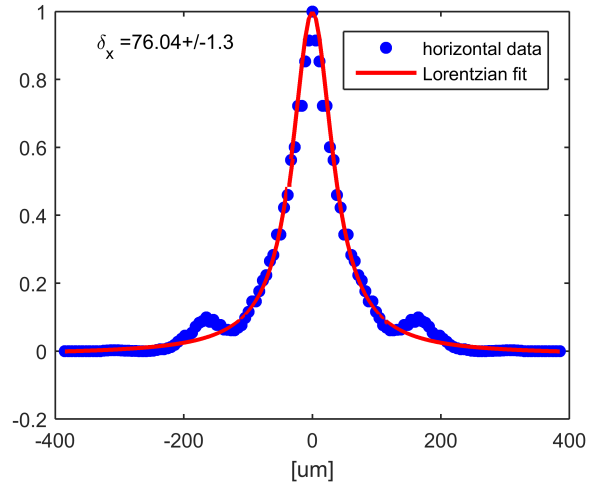

Figure 5.9: Horizontal cut through spatial correlation function with Lorentzian fit and the horizontal speckle size δ_x

As explained in section 5.2, the lens focusses more at higher angle. That means, the speckles are more focused at a higher scattering angle, and therefore smaller in the q space. On the other hand, a longer illumination time had be used to receive an adequate speckle pattern. That triggers a considerable amount of movement in the pattern and a lower contrast. From this point of view, a bigger speckle size is expected. The measured sizes are showing, that the differences are not big enough to make a clear statement. All the analysis above was performed with the effective distance L_{eff} that was calculated with the formfactor analysis. The measured distance between sample and detector is $L_{exp} = 0.094\,\mathrm{m}$. The results are compared in Table 5.1.
The result of this measurement was the determination of a scattering region.
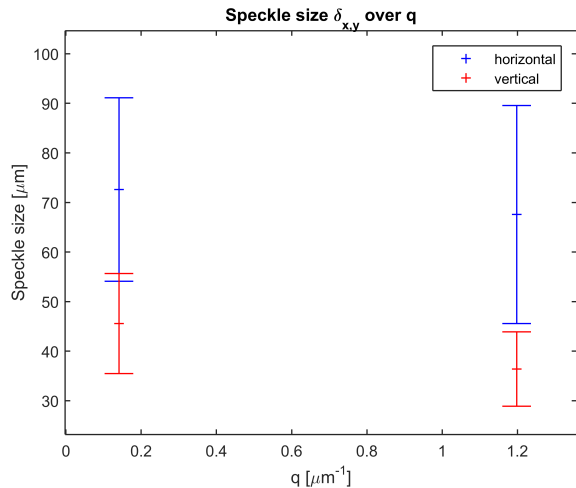
Figure 5.10: Measured speckle sizes $\delta_{x,y}$ in vertical and horizontal dimension at different q values
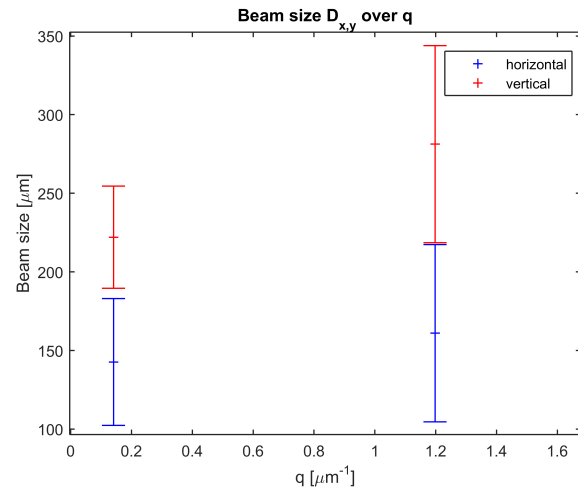
Figure 5.11: Calculated beam sizes $D_{x,y}$ in vertical and horizontal dimension at different q values

Parameter	Value for $\mathbf{L_{eff}}[\mu m]$	Value for $\mathbf{L_{exp}}[\mu m]$
δ_x	72.62 ± 18.51	44.04 ± 11.23
δ_y	45.56 ± 10.09	27.63 ± 6.12
D_x	142.69 ± 40.38	86.54 ± 24.49
D_y	222.04 ± 32.47	134.67 ± 19.69

Table 5.1: Results for speckle size (δ_x, δ_y) and beam size (D_x, D_y) at $q = 0.14 \, \mu\mathrm{m}^{-1}$ for $L_{eff} = 0.155 \, \mathrm{m}$ and $L_{exp} = 0.094 \, \mathrm{m}$

5.5   Double Pulse Correlations

Measurement of colloidal dynamics can be done in two ways with different advantages. The first is the more common method of intensity autocorrelation (see section 2.3). The minimal lag time τ of the correlation function is determined by the camera frame rate. For example a frame acquisition rate of $120 \, \mathrm{Hz}$ equals a lag time of $8.3 \, \mathrm{ms}$. Therefore, the detector determines the fastest particle dynamics that can be traced. For illustration the camera frame rate was set to $5 \, \mathrm{Hz}$ into an acquisition rate regime, were the autocorrelation analysis cannot give a complete result. In Fig.5.12 one can see, that the g_2 function for $4.5 \, \mu\mathrm{m}$ polystyrene particles cannot cover the whole curve to determine the relaxation rate Γ as the fit parameter for Eq.2.23. With Eq.2.30, c_2 data can be plotted together with the autocorrelation plot. With this technique, one gets access to a new time range given by a minimum of twice the pulse width and a maximum given by the camera exposure time. The maximum delay can be made independent of the exposure time, by taking single shot images with a certain delay, now given by the acquisition rate and the sum of two images. This gives the same result, as one image with a double pulse, but only helps in regimes of long delays.

An example of an insufficient $g_2(\mathbf{q}, \tau)$ function is shown in Fig.5.12, which is plotted together with $c_2(\mathbf{q}, \tau)$ data.

The plot shows, that g_2 and c_2 can be fitted with one equation and that even two c_2 data points

can improve the result. One can see in this plot, that the coherence of the setup is particular high, with a β^2 that is ≈ 0.99. During the experiment a dependence of the dynamics on the sample age was recognized. Due to the fact, that the sample should be stored under $4\,^\circ\mathrm{C}$ by the manufacturers restrictions, which was under experimental conditions not possible, the particles possibly created some kind of particle agglomerates after a couple of days. This could be observed by a lot more parasitic scattering in the speckle pattern and lower dynamics. Also a short comparison of a one week old sample with a new one, indicated different particle sizes. This image can be found in the appendix A.2 under Fig.6.4. Therefore, only freshly prepared samples were used for scattering experiments.

In order to validate the theory of Eq.2.30, a set of measurements was done with only delay data at maximal exposure time at $0.39\,\mathrm{Hz}$, to access the full function with contrast analysis data. A frame rate of $0.39\,\mathrm{Hz}$ allows exposure times of $2.5\,\mathrm{s}$ and therefore delay times up to this range. The scattering pattern was measured at three different detector positions and these images were divided into smaller rings, which are in the same q area. Fig.5.13 shows the g_2 function at the maximal q value with a selected 200 pixel wide ring, that equals a width of $0.14\,\mu\mathrm{m}^{-1}$. The maximum q value of $4.3\,\mu\mathrm{m}^{-1}$ is limited by the range of the motor stage in this case.

In Fig.5.13 one can see, that the minimal delay is not on the plateau of the function. Even though, the fit a good approximation in terms of the single shot contrast β^2.

This measurement was carried out for three detector positions and the corresponding images were divided into smaller q values. Fig.5.14 shows three different q rings with a masked out area.
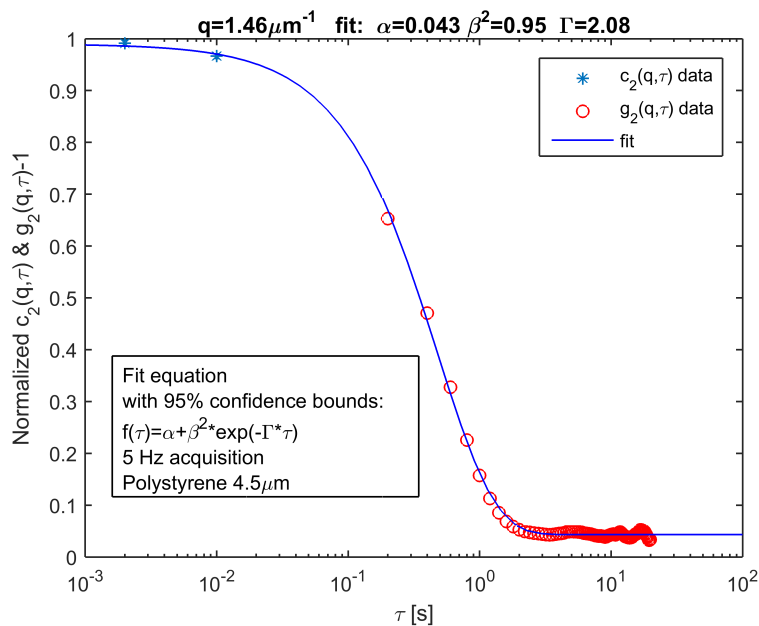
Figure 5.12: g_2 function with fit, autocorrelation data (red) combined with delay data (blue). The plot is an example for an insufficient time range of only autocorrelation data and that the range can be expanded by delay measurements.
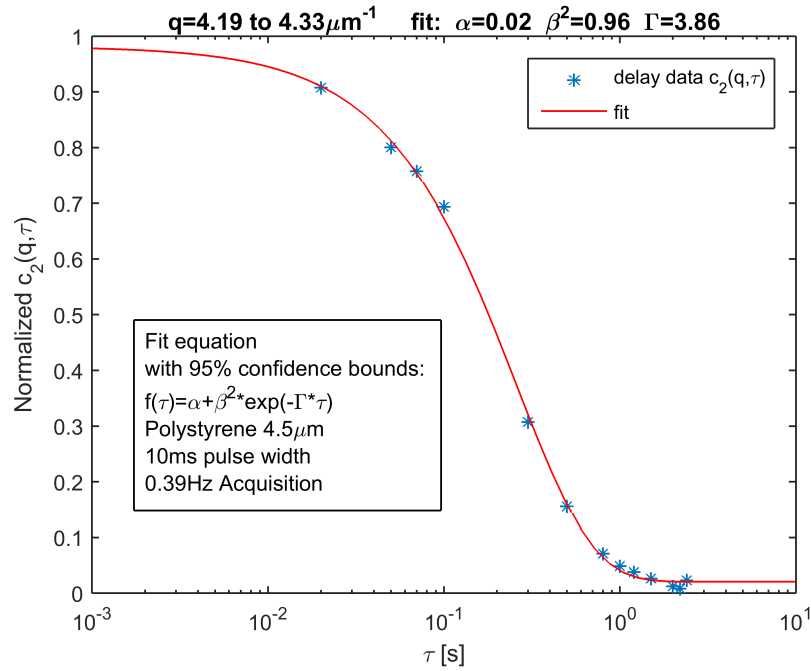
Figure 5.13: g_2 function out of c_2 data points at maximum q-value, divided into a 200 pixel wide q-ring, which equals a width of $0.14\,\mu\mathrm{m}^{-1}$.

The fit result of each ring analysis is plotted in Fig.5.16. The translational diffusion coefficient (D_0) can be determined by the gradient of the linear fit Γ by Eq.2.24. The linear trend of the measurement data indicates Brownian motion of the particles.

The error bars in horizontal direction are showing the uncertainty of the q ring width and in vertical direction the uncertainty of the corresponding g_2 fit. The fit in Fig.5.16 is of good quality with an adjusted R^2-value of $R^2 = 0.994$. With Eq.2.24 the slope is determined by

$$D_0 = (8.346 \pm 0.316) \cdot 10^{-14}\,\mathrm{m}^2/\mathrm{s}$$

with the relaxation rate Γ. With Eq.2.20 at a temperature of $20 \pm 0.1\,°\mathrm{C}$ the approximated viscosity of water $1.003\,\mathrm{mPas}$ [16], the hydrodynamical radius (R_h) can be calculated to

$$R_h = (2.567 \pm 0.097)\,\mu\mathrm{m}.$$

The viscosity of water can be selected, because the sample is very diluted with 5 parts particles to 3000 parts water. This result is close to the manufacturers specification of the polystyrene particles [4], which are

$$R = (2.26 \pm 0.08)\,\mu\mathrm{m}.$$

The result of a slightly higher value is expected, because the manufacturer probably measured the particles in a dried state with a Scanning or Transmission Electron Microscope, which are giving the highest accuracy of a particle size measurement. When the particles are now put into
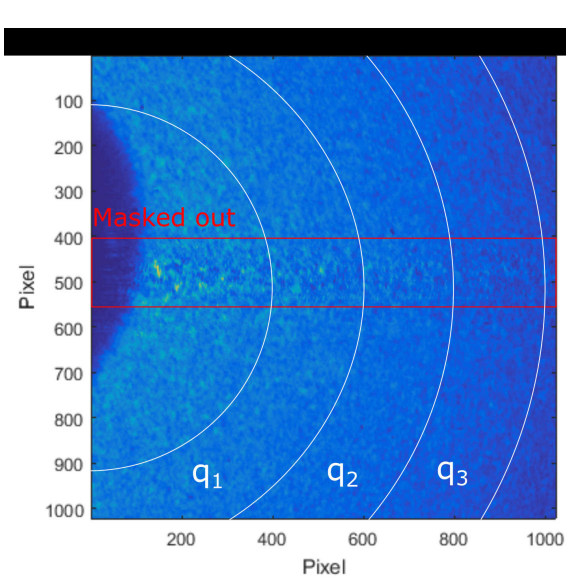
Figure 5.14: Averaged image at small q with three analysis rings and a masked out area.
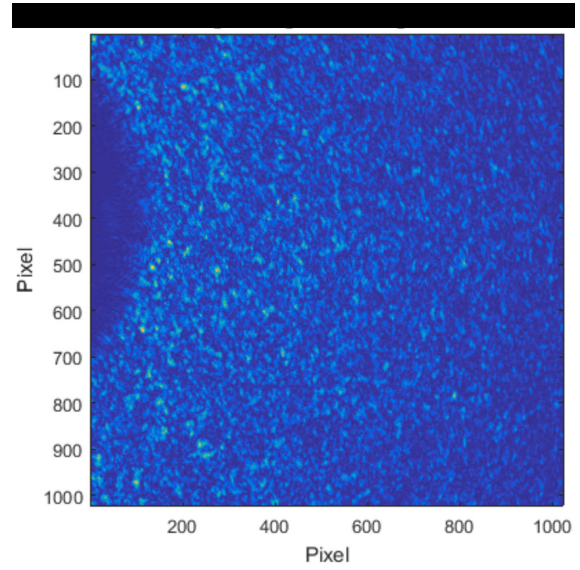
Figure 5.15: Example speckle pattern from a single shot. The static streaks are only visible in the averaged image.

fluid, they may expand a little bit to the hydrodynamical radius R_h.

In conclusion, one can say that the measured particle radius coincides with the specifications in the 4σ range and therefore the correctness of the setup can be seen as successfully verified.
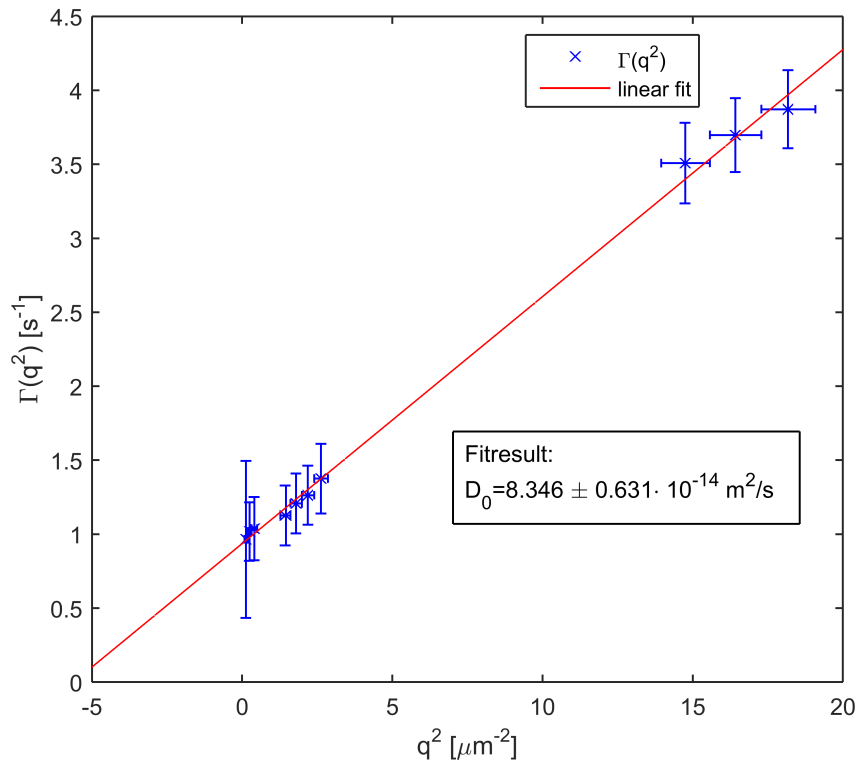

Figure 5.16: Relaxation rate Γ resulted from c_2 function fits over q^2 with linear fit of 95% confidence bounds.

6 Summary and Outlook

A double pulse correlation spectroscopy setup was developed and a measurement with a proof of principle model system of $4.5\,\mu\text{m}$ diameter polystyrene particles verified the functionality of the setup. The process of building underwent several stages with corresponding experiments on the setup's accuracy. These tests have shown, that the experiment of double pulse correlation spectroscopy with visible light was successful.

However there are certain limitations and inefficiencies in the setup. The first limitation is the laser. A higher intensity could give the opportunity to shorten the pulse width to a lower value and to measure even faster dynamics. The AOM also is a factor for the intensity and the time resolution. The response time of the AOM used in this project was around $\sim 1\,\mu\text{s}$. A new concept could be developed using a femtosecond laser source such as Ti:Sapphire laser systems, which can reduce the pulse durations down to the range of femtoseconds [17]. For this range of dynamics, an AOM is insufficient in its response time. A concept like an X-ray delay line [3] could give the possibility to study ultrafast dynamics with visible light. The X-ray delay line is based on splitting the pulse into two paths of different length and to recombine them with a delay based on the length difference of the paths. This concept could be applied with a pulsed laser.

It is also possible, to apply a similar model of an AOM to the X-ray case. With diffraction from surface acoustic waves on quartz crystals, a time resolution up to $100\,\text{ps}$ can be achieved [18]. To access a faster resolution, the split and delay line provides by now, a faster resolution up to $16.7\,\text{ps}$ [3]. The reason for the advantages are for the delay, that it is mostly based on geometry. A difference of $1\,\text{cm}$ in the paths, already produces a delay of $\sim 30\,\text{ps}$ which is currently not accessible with diffraction from crystal surfaces.

To make the setup more efficient and easier to use, one has to improve the software and controls. By now, the CCD motor stage and camera itself are controlled by different computer systems and every measurement step has to be done manually. Therefore, a fully automatic device with maybe a rotational stage and temperature control could highly improve the result of a DLS measurement. Also the current setup could be tested under different conditions. One could analyse a sample which does not follow Brownian dynamics. Even smaller and faster particles can be analysed. With the right instruments, the double pulse method allows a specific and universal characterization of colloidal systems.

List of Figures

List of Tables

Nomenclature and Symbols

DLS   Dynamic Light Scattering

AOM   Acusto-Optic Modulator

DDG   Digital Delay Generator

WFG   Wavefunction Generator

CCD   Charged-Coupled Device camera

q   Scattering Vector

r   Position vector

$g_2(\mathbf{q}, t)$ Intensity autocorrelation function

$c_2(\mathbf{q}, t)$ Double pulse contrast

$f(\mathbf{q}, t)$ Intermediate scattering function

β^2 Single shot contrast

τ Delay time

Γ Relaxation rate

t Time

D_0 translational diffusion coefficient

η (dynamic) Viscosity

T Temperature

k_B Boltzmann constant

R_h hydrodynamical radius

Acknowledgements

A Appendix

A.1 Double pulse speckle contrast

The contrast for a double pulse image over τ is [2]

$$c_2(\mathbf{q}, \tau) = \frac{\langle S^2(\mathbf{q}, \tau)\rangle - \langle S(\mathbf{q}, \tau)\rangle^2}{\langle S(\mathbf{q}, \tau)\rangle^2}. \tag{6.1}$$

$\langle S^2(\mathbf{q}, \tau)\rangle$ can be expressed as

$$\langle S^2(\tau)\rangle = \langle [I(t) + I(t+\tau)] \cdot [I(\mathbf{q}, t) + I(\mathbf{q}, t+\tau)]\rangle = 2\langle I^2\rangle + 2\langle I(\mathbf{q}, t)I(\mathbf{q}, t+\tau)\rangle \tag{6.2}$$

and the squared mean intensity is

$$\langle S(\mathbf{q}, \tau)\rangle^2 = \langle I(\mathbf{q}, t) + I(\mathbf{q}, t+\tau)\rangle^2 = 4\langle I\rangle^2. \tag{6.3}$$

This leads to the double pulse contrast

$$c_2(\mathbf{q}, \tau) = \frac{2\langle I^2\rangle + 2\langle I(\mathbf{q}, t)I(\mathbf{q}, t+\tau)\rangle - 4\langle I\rangle^2}{4\langle I\rangle^2}, \tag{6.4}$$

which can be rewritten with $\sigma^2(I) = \langle I^2\rangle - \langle I\rangle^2$ to

$$c_2(\mathbf{q}, \tau) = \frac{2\sigma^2(I) + 2\langle I(\mathbf{q}, t)I(\mathbf{q}, t+\tau)\rangle - 2\langle I\rangle^2}{4\langle I\rangle^2}. \tag{6.5}$$

Assuming now a fully coherent beam, the normalized variance of the single speckle pattern (β^2) equals 1 and the first term in Eq. 6.5 is

$$\frac{1}{2}\frac{\sigma^2(I)}{\langle I\rangle^2} = \frac{1}{2} \tag{6.6}$$

Using the Siegert relation for Gaussian signals $\langle I(\mathbf{q}, t)I(\mathbf{q}, t+\tau)\rangle/\langle I(\mathbf{q}, t)\rangle^2 = 1 + |f(\mathbf{q}, \tau)|^2$ we write for the second term in Eq.6.5

$$\frac{\langle I(\mathbf{q}, t)I(\mathbf{q}, t+\tau)\rangle}{2\langle I\rangle^2} = \frac{1}{2}\left(1 + |f(\mathbf{q}, \tau)|^2\right), \tag{6.7}$$

where $f(\mathbf{q}, \tau)$ is the intermediate scattering function. The first term cancels the last term in Eq.6.5 and therefore only the middle term Eq.6.7 is left. So we can express the normalized speckle contrast as

$$c_2(\mathbf{q}, \tau) = \frac{1}{2}\left(1 + |f(\mathbf{q}, \tau)|^2\right). \tag{6.8}$$
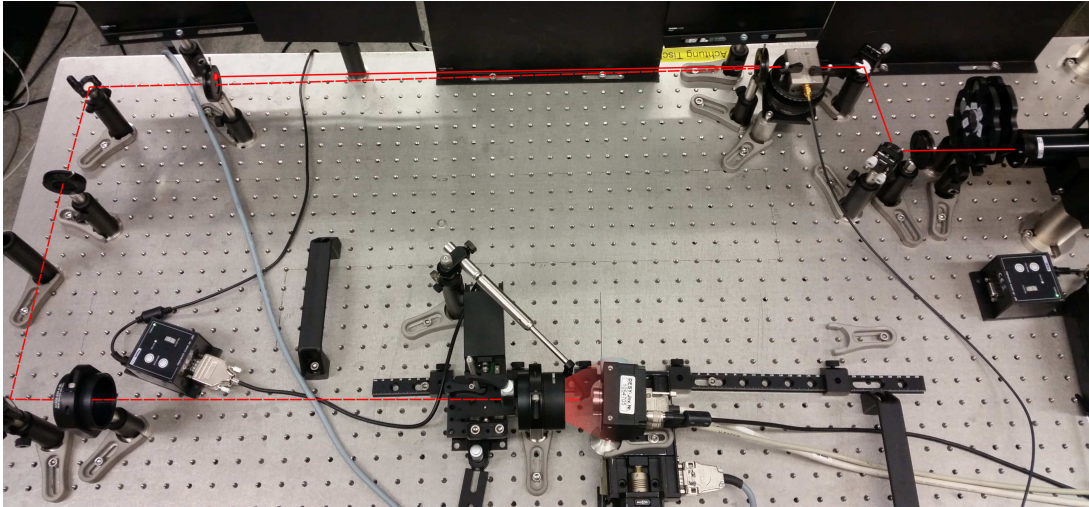
A.2 Double pulse setup

Figure 6.1: Setup image with beam drawn inside, without the black box.
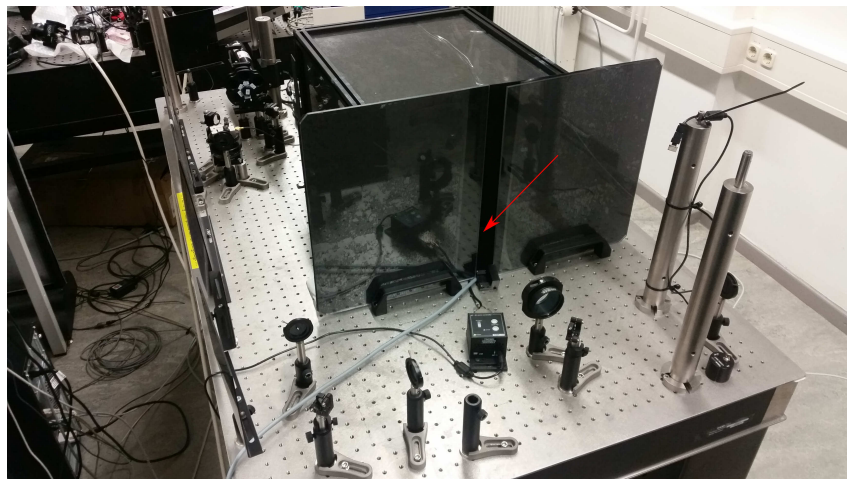

Figure 6.2: Setup with the black box and optical table from above. The beam enters on the front side through an aperture (red arrow).
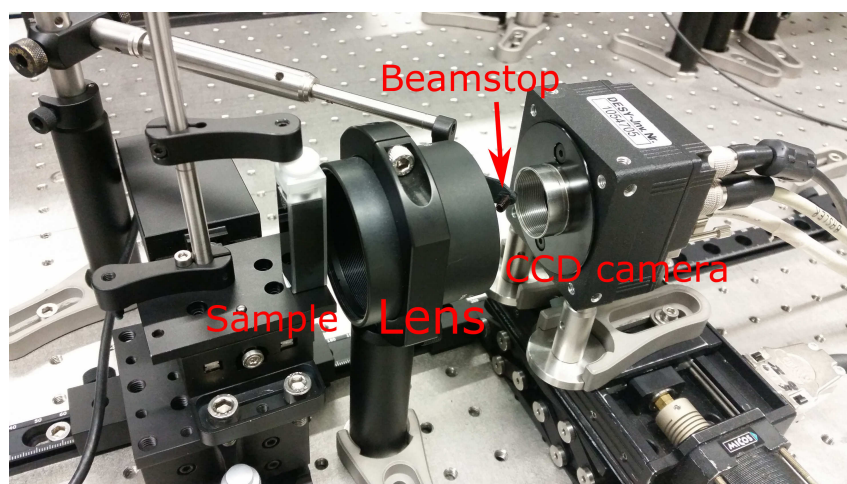
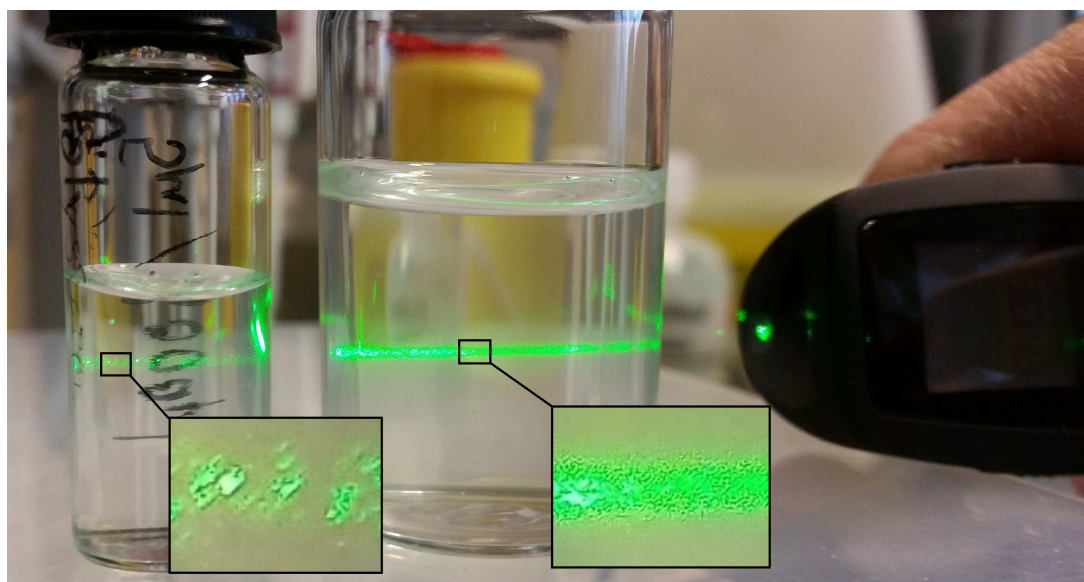Figure 6.3: Sample holder, lens and movable CCD inside of the black box.

Figure 6.4: Example for an already decayed polystyrene sample on the left and a new prepared one on the right. The big particles on the left are visible to the eye, while the right solution is more uniform distributed.

References

[1] B.J. Berne and R. Pecora. *Dynamic Light Scattering: With Applications to Chemistry, Biology, and Physics*. Dover Publications, Mineola, 2000.

[2] C. Gutt, L.-M. Stadler, A. Duri, T. Autenrieth, O. Leupold, Y. Chushkin, and G. Grübel. *Opt. Express*, 17(1):55–61, 2009.

[3] W. Roseker, H. Franz, H. Schulte-Schrepping, A. Ehnes, O. Leupold, F. Zontone, A. Robert, and G. Grübel. *Opt. Lett.*, 34(12):1768–1770, 2009.

[4] Polyscience, Inc. Polybead® Microspheres 4.50μm (http://www.polysciences.com/default/polybead-microspheres-450181m).

[5] G. Grübel and F. Zontone. *J. Alloys Compd.*, 362(1 - 2):3 – 11, 2004. Proceedings of the Sixth International School and Symposium on Synchrotron Radiation in Natural Science (ISSRNS).

[6] J.W. Goodman. *Speckle Phenomena in Optics, Theory and Applications*. Roberts & Company, 2007.

[7] Thorlabs GmbH. HNL050R-EC Spec Sheet (http://www.thorlabs.de/thorcat/22100/HNL050R-EC-SpecSheet.pdf).

[8] Thorlabs GmbH. CV10Q700S - 700 μL Micro Cuvette with Stopper, 2 Pack (https://www.thorlabs.de/thorproduct.cfm?partnumber=CV10Q700S).

[9] Basler AG. User's manual for camera link cameras, Basler Aviator AW000830 (http://s.baslerweb.com/media/documents/AW00083008000%20Aviator%20Camera%20Link%20Users%20Manual.pdf).

[10] Gooch & Housego GmbH. I-M110-2C10B6-3-GH26 Acousto-Optic Modulator Data Sheet (http://www.goochandhousego.com/wp-content/uploads/2013/12/IWDS025-V1.0-I-M110-2C10B6-3-GH26-AOM.pdf).

[11] J. Kim, J. Sohn, Y. Jo, H. Woo, J. Han, S. Cho, A.I. Inamdar, H. Kim, and H. Im. *Journal of the Korean Physical Society*, 65(9):1320–1323, 2014.

[12] A. Robert. *Dynamic Behavior or Charge Stabilized Colloidal Suspensions*. PhD thesis, Universite Joseph Fourier-Grenoble, 2001.

[13] J. Wagner, W. Härtl, and R. Hempelmann. *Langmuir*, 16(9):4080–4085, 2000.

[14] M. Kotlarchyk and H. Chen. *J. Chem. Phys.*, 79(5):2461–2469, 1983.

[15] C. Gutt, P. Wochner, B. Fischer, H. Conrad, M. Castro-Colin, S. Lee, F. Lehmkühler, I. Steinke, M. Sprung, W. Roseker, D. Zhu, H. Lemke, S. Bogle, P. H. Fuoss, G. B.

Stephenson, M. Cammarata, D. M. Fritz, A. Robert, and G. Grübel. *Phys. Rev. Lett.*, 108:024801, 2012.

[16] http://www.thermexcel.com/english/tables/eau_atm.htm.

[17] S. Lee, W. Jo, H. Sub Wi, C. Gutt, and G. Woo Lee. *Opt. Express*, 22(18):21567–21576, 2014.

[18] R. Tucoulou, D. V. Roshchupkin, O. Mathon, I. A. Schelokov, M. Brunel, E. Ziegler, and C. Morawe. *J. Synchrotron Radiat.*, 5(6):1357–1362, 1998.